Application of numerical bifurcation tracking strategy to blade-tip/casing interactions in aircraft engines

Clément Delbé, Yann Colaïtis, Alain Batailly

POLYTECHNIQUE MONTRÉAL
UNIVERSITÉ D'INGÉNIERIE

LABORATOIRE D'ANALYSE VIBRATOIRE ET ACOUSTIQUE

Application of numerical bifurcation tracking strategy to blade-tip/casing interactions in aircraft engines

C. Delbé[1], Y. Colaïtis[1], A. Batailly[1]

Abstract

Building on the regularized-Lanczos harmonic balance method, a previously developed frequency method, this paper presents a numerical bifurcation tracking strategy dedicated to high-dimensional nonlinear mechanical systems. In order to demonstrate its applicability to industrial applications, it is here used to obtain original results in the context of blade-tip/casing interactions in aircraft engines. The emphasis is put specifically on the tracking of predicted limit point bifurcations as key parameters—such as the amplitude of the aerodynamic forcing applied on the blade, the friction coefficient or the operating clearances—vary. Overall, presented results underline that the employed frequency method is well-suited to tackle the numerical challenges inherent to such computations on high-dimensional systems. For the mechanical system of interest, the industrial fan blade NASA rotor 67, it is shown that the application of the presented strategy yields an efficient way to identify isolated branches of solutions, which may be of critical importance from a design standpoint.

Keywords

harmonic balance method; blade-tip/casing contacts; rotor/stator interaction; bifurcation tracking; isolated branches of solutions

1 - Département de génie mécanique, École Polytechnique de Montréal, P.O. Box 6079, Succ. Centre-Ville, Montréal, Québec, Canada H3C 3A7

Application d'une stratégie numérique de suivi de bifurcation au contact aube/carter dans les moteurs d'avion

C. Delbé[1], Y. Colaïtis[1], A. Batailly[1]

Résumé

S'appuyant sur la méthode de l'équilibrage harmonique avec filtrage de Lanczos et régularisation de la loi de contact, une méthode déjà présentée dans la littérature, cet article présente une procédure de suivi de bifurcation adaptée à des systèmes non linéaires de grande dimension. Afin de démontrer la pertinence de cette procédure à des configurations industrielles, il est montré que son application à un cas de contact aube/carter dans les moteurs d'avion permet d'obtenir des résultats originaux. Une attention particulière est portée au suivi des points limites en faisant varier certains paramètres clé du système (tels que l'amplitude du forçage aérodynamique, le coefficient de frottement ou encore les jeux en fonctionnement). Dans l'ensemble, les résultats présentés démontrent que la procédure permet de remédier à certains défis numériques inhérents aux systèmes non linéaires de grande dimension. Plus précisément, dans le cadre de son application sur une aube de soufflante industrielle (aube NASA rotor 67), cette procédure permet de détecter de nouvelles branches de solutions isolées pouvant être d'un grand intérêt pour les concepteurs.

Mots-clés

méthode de l'équilibrage harmonique; contacts aube/carter; interaction rotor/stator; suivi de bifurcation; branches de solutions isolées

1 - Département de génie mécanique, École Polytechnique de Montréal, P.O. Box 6079, Succ. Centre-Ville, Montréal, Québec, Canada H3C 3A7

1 Introduction

In a competitive global economy, the evolution of environmental norms calls for innovative design strategies. For aircraft engine manufacturers in particular, this implies pushing the boundaries of structural design so as to account for nonlinear structural interactions that have long been mitigated at the expense of the engine overall efficiency. Over the past years, considerable research efforts were made to better understand, model and predict nonlinear structural interactions, be it at the blade/underplatform damper [1, 2, 3], the rotor/bearing [4, 5] or the blade-tip/casing [6, 7, 8, 9, 10, 11, 12, 13, 14, 15] interfaces. Because these nonlinear interactions directly impact the modal properties of structural com- ponents, it is essential to account for them in early design stages.

Among the aforementioned nonlinear interfaces, nonlinear phenomena resulting from contacts along the blade-tip/casing interface are still motivating researchers to develop solution methods [15, 16, 17] and full-scale experimental facilities [7, 10, 12, 14, 18]. Indeed, the severity of contact events at this interface—related to the combination of very high relative speeds, extreme thermal conditions and complex wear phenomena—yields a variety of sophisticated interactions that may involve a single blade, a full bladed disk and even the surrounding casing.

Recently, a numerical frequency method, namely the regularized-Lanczos harmonic balance method (RL-HBM), has been developed and successfully applied to the qualitative analysis of blade-tip/casing interactions [15]. While obtained results were shown to be perfectly in line with those obtained with time integration techniques, the RL-HBM is able to efficiently predict nonlinear resonances, which may be computationally challenging with time integration techniques. It was also later shown that the RL-HBM is well suited to efficiently assess the stability of predicted solutions and detect bifurcation points [19]. Knowing the location of bifurcation points is an essential piece of information to determine the stability of the different branches of nonlinear solutions and therefore knowing the stability limits of the system. There are several types of bifurcations, each associated with a qualitative change in the characteristics of the system of interest. (1) Limit Point (LP) bifurcations, where the nonlinear frequency response curve (NFRC) features a vertical tangent, refer to a change in stability between two solution branches. (2) Branch Point (BP) bifurcations refer either to the loss of stability of a branch of solutions and to the birth of a new stable branch, or conversely. Finally, (3) Neimark-Sacker (NS) bifurcations are associated with a transition from periodic to quasiperiodic regimes.

Even without carrying out a stability analysis, in the context of a design process, the computational cost of frequency analyses for different values of key parameters—be it the amplitude of the aerodynamic forcing applied on the blade, the friction coefficient or the operating clearances for instance—may still constitute a significant roadblock. From a general perspective, the idea of assessing the influence of a given parameter on nonlinear frequency response curves has long been investigated. In fact, bifurcation points vary in a complex way in the global parametric space of resolution and, in order to increase the knowledge of the stability limits, it would therefore be relevant to track the bifurcation points in a parametric space augmented by a second control parameter. To this end, numerical methods have been developed to track specific solutions [20] in a parametric space, such as limit point (LP) [21, 22, 23] and other types of bifurcations [21, 22, 24]. It is therefore possible to track a bifurcation in the parametric space depending on a given physical parameter such as the amplitude of the aerodynamic forcing applied on the blade, the friction coefficient or the operating clearances.

Bifurcation tracking is here extended to the RL-HBM. It is underlined that the RL-HBM (that features contact regularization and Lanczos filtering of the contact forces) is particularly well-suited for bifurcation tracking and the detection of isolated branches of solutions. It provides an efficient numerical framework in which original blade-tip/casing interaction phenomena are numerically predicted. To the best of the authors' knowledge, it is the first time that bifurcation tracking is successfully applied on industrial systems in the context of blade-tip/casing contact problems. This paper specifically focuses on the tracking of LP bifurcations, under the assumption that a blade's response to blade-tip/casing contacts is periodic. In the literature, proposed methodologies for such bifurcation tracking are usually applied to low-dimensional academic systems, featuring 1 or 2 degrees of freedom [21, 22, 23, 25]. While such systems may exhibit a very rich dynamics, they are associated to fast computation times and the application of bifurcation tracking on these systems usually does not yield the same numerical challenges as high-dimensional systems. That is the reason why, attention is paid to underline that the proposed strategy is well-suited for an industrial application. Indeed, the present article provides results obtained from the application of bifurcation tracking to a 39-dof (including 27 nonlinear dof) reduced-order model of an industrial fan blade (NASA

Rotor 67, which finite element mesh contains more than 10^5 dof). Section 2 presents the methodology of the HBM and section 3 that of the bifurcation tracking. Section 4 presents the model of interest and the results obtained are presented in section 5.

2 Numerical framework

A n-degree of freedom (dof) nonlinear mechanical system (S), characterized by its mass, damping and stiffness matrix, denoted respectively $\mathbf{M}$, $\mathbf{C}$ and $\mathbf{K}$ (all of dimensions $n \times n$) is considered. For a given time t, the n-dimensional column vectors of displacement, nonlinear forces and external forces are respectively denoted $\boldsymbol{x}(t) = [x_1, \ldots, x_n]$, $\boldsymbol{f}_{\text{nl}}(\omega, \boldsymbol{x}, \dot{\boldsymbol{x}}) = [f_{\text{nl},1}, f_{\text{nl},2}, \ldots, f_{\text{nl},n}]$ and $\boldsymbol{f}_{\text{ext}}(\omega, t) = [f_{\text{ext},1}, f_{\text{ext},2}, \ldots, f_{\text{ext},n}]$. The normalized equation of motion reads:

$$\frac{\alpha}{\beta^2}\mathbf{M}\ddot{\boldsymbol{x}}(t) + \frac{\alpha}{\beta}\mathbf{C}\dot{\boldsymbol{x}}(t) + \alpha\mathbf{K}\boldsymbol{x}(t) + \boldsymbol{f}_{\text{nl}}\left(\omega, \boldsymbol{x}, \dot{\boldsymbol{x}}\right) = \boldsymbol{f}_{\text{ext}}\left(\omega, t\right) \tag{1}$$

The space and time normalization coefficients, α and β, are calculated such that $\|\alpha\boldsymbol{x}(t)\| \simeq 1$ and $\omega/\beta \simeq 1$. Derivatives with respect to time t are marked with overdots.

2.1 Harmonic balance method

The harmonic balance method (HBM) [26, 27] is a frequency method to solve the nonlinear differential system (1). It relies on the assumption that the solution $\boldsymbol{x}(t)$ is periodic and may thus be developped into Fourier series. Therefore, $\boldsymbol{x}(t)$, $\boldsymbol{f}_{\text{nl}}(\omega, \boldsymbol{x}, \dot{\boldsymbol{x}})$ and $\boldsymbol{f}_{\text{ext}}(\omega, t)$ can be written:

$$\begin{aligned}
\boldsymbol{x}(t) &\simeq \frac{1}{2}\boldsymbol{a}_0 + \sum_{j=1}^{H}\left[\boldsymbol{a}_j \cos\left(j\omega t\right) + \boldsymbol{b}_j \sin\left(j\omega t\right)\right] \\
\boldsymbol{f}_{\text{nl}}(\omega, \boldsymbol{x}, \dot{\boldsymbol{x}}) &\simeq \frac{1}{2}\boldsymbol{a}_0^{\text{nl}} + \sum_{j=1}^{H}\left[\boldsymbol{a}_j^{\text{nl}} \cos\left(j\omega t\right) + \boldsymbol{b}_j^{\text{nl}} \sin\left(j\omega t\right)\right] \\
\boldsymbol{f}_{\text{ext}}(\omega, t) &\simeq \frac{1}{2}\boldsymbol{a}_0^{\text{ext}} + \sum_{j=1}^{H}\left[\boldsymbol{a}_j^{\text{ext}} \cos\left(j\omega t\right) + \boldsymbol{b}_j^{\text{ext}} \sin\left(j\omega t\right)\right]
\end{aligned} \tag{2}$$

with $\boldsymbol{a}_j^{\mathcal{E}}$ and $\boldsymbol{b}_j^{\mathcal{E}}$, $\mathcal{E} \in \{., \text{nl}, \text{ext}\}$, the n-dimensional column vectors of real Fourier coefficients $a_j^{\mathcal{E},i}$ and $b_j^{\mathcal{E},i}$ for each dof $i \in [1, n]$. The $2H+1$-dimensional row vector of the Fourier basis associated with the decomposition (2) is introduced:

$$\mathbb{T}_H = \left[\frac{1}{2}, \cos\left(\omega t\right), \sin\left(\omega t\right), \ldots, \cos(H\omega t), \sin(H\omega t)\right] \tag{3}$$

Time quantities $\boldsymbol{x}(t)$, $\boldsymbol{f}_{\text{nl}}(\omega, \boldsymbol{x}, \dot{\boldsymbol{x}})$ and $\boldsymbol{f}_{\text{ext}}(\omega, t)$ are written in the frequency domain using the Kronecker product $\otimes$:

$$\begin{aligned}
\boldsymbol{x}(t) &= \left(\mathbb{T}_H \otimes \mathbf{I}_n\right)\tilde{\boldsymbol{x}} \\
\boldsymbol{f}_{\text{nl}}(\omega, \boldsymbol{x}, \dot{\boldsymbol{x}}) &= \left(\mathbb{T}_H \otimes \mathbf{I}_n\right)\tilde{\boldsymbol{f}}_{\text{nl}} \\
\boldsymbol{f}_{\text{ext}}(\omega, t) &= \left(\mathbb{T}_H \otimes \mathbf{I}_n\right)\tilde{\boldsymbol{f}}_{\text{ext}}
\end{aligned} \tag{4}$$

where $\tilde{\boldsymbol{x}}$, $\tilde{\boldsymbol{f}}_{\text{nl}}$ and $\tilde{\boldsymbol{f}}_{\text{ext}}$ are column vectors containing the $n_H = n(2H+1)$ coefficients of the Fourier decomposition:

$$\begin{aligned}
\tilde{\boldsymbol{x}} &= \left[\boldsymbol{a}_0, \boldsymbol{a}_1, \boldsymbol{b}_1, \ldots, \boldsymbol{a}_H, \boldsymbol{b}_H\right]^\top \\
\tilde{\boldsymbol{f}}_{\text{nl}} &= \left[\boldsymbol{a}_0^{\text{nl}}, \boldsymbol{a}_1^{\text{nl}}, \boldsymbol{b}_1^{\text{nl}}, \ldots, \boldsymbol{a}_H^{\text{nl}}, \boldsymbol{b}_H^{\text{nl}}\right]^\top \\
\tilde{\boldsymbol{f}}_{\text{ext}} &= \left[\boldsymbol{a}_0^{\text{ext}}, \boldsymbol{a}_1^{\text{ext}}, \boldsymbol{b}_1^{\text{ext}}, \ldots, \boldsymbol{a}_H^{\text{ext}}, \boldsymbol{b}_H^{\text{ext}}\right]^\top
\end{aligned} \tag{5}$$

Velocity and acceleration vectors, respectively $\dot{\boldsymbol{x}}(t)$ and $\ddot{\boldsymbol{x}}(t)$, are also calculated from $\tilde{\boldsymbol{x}}$ and the derivation operator from the base $\mathbb{T}_H$, denoted $\boldsymbol{\nabla}$:

$$\boldsymbol{\nabla} = \text{diagblock}\left(0, \boldsymbol{\nabla}_1, \ldots, \boldsymbol{\nabla}_j, \ldots, \boldsymbol{\nabla}_H\right) \tag{6}$$

with $\boldsymbol{\nabla}_j$, the first derivation matrix of the j^{th} harmonic:

$$\boldsymbol{\nabla}_j = j \begin{bmatrix} 0 & 1 \\ -1 & 0 \end{bmatrix} \quad \text{for} \quad j \in [\![1, H]\!] \tag{7}$$

hence:

$$\begin{aligned} \dot{\boldsymbol{x}}(t) &= \omega \left[\left(\mathbb{T}_H \boldsymbol{\nabla}\right) \otimes \mathbf{I}_n\right] \tilde{\boldsymbol{x}} \\ \ddot{\boldsymbol{x}}(t) &= \omega^2 \left[\left(\mathbb{T}_H \boldsymbol{\nabla}^2\right) \otimes \mathbf{I}_n\right] \tilde{\boldsymbol{x}} \end{aligned} \tag{8}$$

Rewriting Eq.(1) with frequency variables and applying a Galerkin procedure [28, 29] to eliminate the time dependence of the approximation functions, a nonlinear algebraic system of n_H equations is obtained:

$$\mathbf{r}(\tilde{\boldsymbol{x}}, \omega) = \mathbf{Z}(\omega)\tilde{\boldsymbol{x}} + \tilde{\boldsymbol{f}}_{\text{nl}}(\tilde{\boldsymbol{x}}) - \tilde{\boldsymbol{f}}_{\text{ext}}(\omega) = \mathbf{0}_{n_H} \tag{9}$$

with $\mathbf{Z}(\omega)$ the dynamic stiffness matrix of dimension $n_H \times n_H$:

$$\mathbf{Z}(\omega) = \omega^2 \boldsymbol{\nabla}^2 \otimes \mathbf{M} + \omega \boldsymbol{\nabla} \otimes \mathbf{C} + \mathbf{I}_{2H+1} \otimes \mathbf{K} \tag{10}$$

For the sake of computational efficiency, a classical block condensation involving the Schur complement is used to reduce the size of the algebraic system (9) to $q_H = q(2H+1)$ where q is the number of nonlinear dof. The nonlinear reduced algebraic system of q_H equations whose q_H unknowns are the Fourier coefficients contained in the vector $\tilde{\boldsymbol{x}}^{\text{nl}}$ is therefore written:

$$\mathbf{R}(\tilde{\boldsymbol{x}}^{\text{nl}}, \omega) = \mathbf{Z}_{\text{red}}(\omega)\tilde{\boldsymbol{x}}^{\text{nl}} + \tilde{\boldsymbol{f}}_{\text{nl,red}}\left(\tilde{\boldsymbol{x}}^{\text{nl}}, \omega\right) - \tilde{\boldsymbol{f}}_{\text{ext,red}}(\omega) = \mathbf{0}_{q_H} \tag{11}$$

2.2 Arc-length continuation

The computation of the nonlinear frequency response curve (NFRC) over a range of pulsation ω requires a continuation procedure. In this paper, the arc-length continuation technique based on a prediction-correction scheme is used [15]. The arc-length continuation consists in imposing that the arc length between the converged solution $\mathbf{X}_{i-1}$ and the prediction $\mathbf{X}_i^{k=0}$ is equal to δs during the correction step. Thus, the control parameter ω therefore becomes an unknown of the problem and the augmented unknown vector becomes $\mathbf{X} = \left[\tilde{\boldsymbol{x}}^{\text{nl}}, \omega\right]^\top$.

2.2.1 Prediction

The calculation of a solution $\mathbf{X}_i$ relies on an iterative Newton-Raphson procedure, an initial estimate $\mathbf{X}_i^0$ is therefore required. The latter can be calculated by different prediction techniques [15], the secant prediction is here considered. For $i \geq 2$, the prediction of the solution i is calculated from the converged solutions $i-1$ and $i-2$:

$$\mathbf{X}_i^0 = \mathbf{X}_{i-1} + \delta s \frac{\Delta \mathbf{X}_{i-1}}{\|\Delta \mathbf{X}_{i-1}\|} \text{ with } \Delta \mathbf{X}_{i-1} = \mathbf{X}_{i-1} - \mathbf{X}_{i-2} \tag{12}$$

For $\mathbf{X}_0 = \left[\tilde{\boldsymbol{x}}_0^{\text{nl}}, \omega_0\right]^\top$, the prediction $\mathbf{X}_0^0$ is chosen such as $\omega_0 = \omega_{\text{start}}$ and $\tilde{\boldsymbol{x}}_0^{\text{nl}} = \mathbf{0}_{q_H}$ or, in the case where there exists a guess for $\tilde{\boldsymbol{x}}_0^{\text{nl}}$, this guess may be used as a prediction. For $\mathbf{X}_1 = \left[\tilde{\boldsymbol{x}}_1^{\text{nl}}, \omega_1\right]^\top$, the prediction results from the converged solution $\mathbf{X}_0$. So it comes $\mathbf{X}_1^0 = \left[\tilde{\boldsymbol{x}}_0^{\text{nl}}, \omega_0 + \delta\omega\right]^\top$ where $\delta\omega$ is the pulsation increment.

2.2.2 Parameterization

Given the control parameter ω, the parameterization equation $\mathcal{P}(\tilde{\boldsymbol{x}}^{\mathrm{nl}}, \omega, s) = 0$ makes it possible to define the system (13) consisting of $q_H + 1$ equations:

$$\begin{cases} \mathbf{R}(\tilde{\boldsymbol{x}}^{\mathrm{nl}}, \omega) = \mathbf{0}_{q_H} \\ \mathcal{P}(\tilde{\boldsymbol{x}}^{\mathrm{nl}}, \omega, s) = 0 \end{cases} \tag{13}$$

$\mathbf{X}_i^k$ are therefore located on the hypersphere $\mathbb{R}^{q_H+1}$ of radius δs centered in $\mathbf{X}_{i-1}$. Thus, the converged solution $\mathbf{X}_i$ is located at the intersection of the curve $\mathbf{R}(\tilde{\boldsymbol{x}}^{\mathrm{nl}}, \omega) = \mathbf{0}_{q_H}$ and the hypersphere $\mathbb{R}^{q_H+1}$ of radius δs centered at $\mathbf{X}_{i-1}$ [15].

$$\mathcal{P}\left(\tilde{\boldsymbol{x}}_i^{\mathrm{nl},k}, \omega_i^k, s\right) = \left\| \tilde{\boldsymbol{x}}_i^{\mathrm{nl},k} - \tilde{\boldsymbol{x}}_{i-1}^{\mathrm{nl}} \right\|^2 + \left(\omega_i^k - \omega_{i-1}\right)^2 - \delta s^2 = 0 \tag{14}$$

2.2.3 Correction

This step corresponds to the solution of the nonlinear algebraic system (13). $\mathbf{X}_i^{k+1}$ is calculated from $\mathbf{X}_i^k$ using an iterative Newton-Raphson procedure such that $\mathbf{X}_i^{k+1} = \mathbf{X}_i^k + \delta\mathbf{X}_i^k$ with:

$$\begin{bmatrix} \mathbf{R}_{,\tilde{\boldsymbol{x}}^{\mathrm{nl}}}\left(\mathbf{X}_i^k\right) & \mathbf{R}_{,\omega}\left(\mathbf{X}_i^k\right) \\ \mathcal{P}_{,\tilde{\boldsymbol{x}}^{\mathrm{nl}}}^{\top}\left(\mathbf{X}_i^k, s\right) & \mathcal{P}_{,\omega}\left(\mathbf{X}_i^k, s\right) \end{bmatrix} \delta\mathbf{X}_i^k = \begin{bmatrix} -\mathbf{R}\left(\mathbf{X}_i^k\right) \\ -\mathcal{P}\left(\mathbf{X}_i^k, s\right) \end{bmatrix} \tag{15}$$

The prediction $\mathbf{X}_i^{k=0}$ obtained by the secant method (2.2.2) provides a suitable initial guess for the Newton-Raphson procedure. The stopping criterion (16) relating to the approximation error $\mathbf{R}(\tilde{\boldsymbol{x}}^{\mathrm{nl}}, \omega)$ makes it possible to end the iterative process. The tolerance ε will be chosen depending on the model studied.

$$\left\| \mathbf{R}\left(\tilde{\boldsymbol{x}}^{\mathrm{nl}}, \omega\right) \right\| \leq \varepsilon \tag{16}$$

2.3 Alternating Frequency/Time procedure

2.3.1 Nonlinear forces

In the nonlinear algebraic system (11), the vector of nonlinear forces $\tilde{\boldsymbol{f}}_{\mathrm{nl,red}}\left(\tilde{\boldsymbol{x}}^{\mathrm{nl}}, \omega\right)$ must be determined. To do so, the Alterning Frequency/Time (AFT) [30] procedure is adopted.

First, the frequency variable $\tilde{\boldsymbol{x}}^{\mathrm{nl}}$ is mapped onto the time domain by means of an inverse Discrete Fourier Transform (DFT) [31] with the $\boldsymbol{\Gamma}$ operator [22, 23, 29]. This allows to compute the time variables $\boldsymbol{x}(t)$ and $\dot{\boldsymbol{x}}(t)$. A period is discretized into N uniformly distributed instants $\tau_i = \omega t_i = 2i\pi/N$ with $i \in [\![0, N-1]\!]$.

$$\begin{aligned} \boldsymbol{\Gamma} = \Bigg[& \mathbf{I}_q \otimes \begin{bmatrix} 1/2 \\ \vdots \\ 1/2 \end{bmatrix} \quad \mathbf{I}_q \otimes \begin{bmatrix} \cos(\tau_0) \\ \vdots \\ \cos(\tau_{N-1}) \end{bmatrix} \quad \mathbf{I}_q \otimes \begin{bmatrix} \sin(\tau_0) \\ \vdots \\ \sin(\tau_{N-1}) \end{bmatrix} \quad \dots \\ & \dots \quad \mathbf{I}_q \otimes \begin{bmatrix} \cos(H\tau_0) \\ \vdots \\ \cos(H\tau_{N-1}) \end{bmatrix} \quad \mathbf{I}_q \otimes \begin{bmatrix} \sin(H\tau_0) \\ \vdots \\ \sin(H\tau_{N-1}) \end{bmatrix} \Bigg] \end{aligned} \tag{17}$$

hence

$$\begin{aligned} \boldsymbol{x}(t) &= \boldsymbol{\Gamma}\tilde{\boldsymbol{x}}^{\mathrm{nl}} \\ \dot{\boldsymbol{x}}(t) &= \omega\boldsymbol{\Gamma}\left(\boldsymbol{\nabla} \otimes \mathbf{I}_q\right)\tilde{\boldsymbol{x}}^{\mathrm{nl}} \end{aligned} \tag{18}$$

Knowing the time variables $\boldsymbol{x}$ and $\dot{\boldsymbol{x}}$, the qN-vector $\boldsymbol{f}_{\mathrm{nl,red}}(\boldsymbol{x}, \dot{\boldsymbol{x}})$, containing the N steps of the nonlinear forces for each of the q nonlinear dof, is calculated analytically. Finally, the frequency variable $\tilde{\boldsymbol{f}}_{\mathrm{nl,red}}\left(\tilde{\boldsymbol{x}}^{\mathrm{nl}}, \omega\right)$ is obtained

from the time variable $\boldsymbol{f}_{\text{nl,red}}(\boldsymbol{x}, \dot{\boldsymbol{x}})$ using a forward DFT with the $\boldsymbol{\Gamma}^{-1}$ operator:

$$\boldsymbol{\Gamma}^{-1} = \frac{2}{N} \begin{bmatrix} \mathbf{I}_q \otimes & [1 & \dots & 1] \\ \mathbf{I}_q \otimes & [\cos(\tau_0) & \dots & \cos(\tau_{N-1})] \\ \mathbf{I}_q \otimes & [\sin(\tau_0) & \dots & \sin(\tau_{N-1})] \\ & & \vdots & \\ \mathbf{I}_q \otimes & [\cos(H\tau_0) & \dots & \cos(H\tau_{N-1})] \\ \mathbf{I}_q \otimes & [\sin(H\tau_0) & \dots & \sin(H\tau_{N-1})] \end{bmatrix} \tag{19}$$

hence

$$\tilde{\boldsymbol{f}}_{\text{nl,red}} = \boldsymbol{\Gamma}^{-1} \boldsymbol{f}_{\text{nl,red}} \tag{20}$$

2.3.2 Jacobian and derivatives

In order to compute $\delta \mathbf{X}_i^k$, one must solve the algebraic system (15) in which appears the Jacobian matrix $\mathbf{R}_{,\tilde{\boldsymbol{x}}^{\text{nl}}}\left(\mathbf{X}_i^k\right)$:

$$\mathbf{R}_{,\tilde{\boldsymbol{x}}^{\text{nl}}}\left(\mathbf{X}_i^k\right) = \frac{\partial \mathbf{R}}{\partial \tilde{\boldsymbol{x}}^{\text{nl}}}\left(\mathbf{X}_i^k\right) = \mathbf{Z}_{\text{red}}(\omega) + \frac{\partial \tilde{\boldsymbol{f}}_{\text{nl,red}}}{\partial \tilde{\boldsymbol{x}}^{\text{nl}}}\left(\mathbf{X}_i^k\right) \tag{21}$$

To compute $\mathbf{R}_{,\tilde{\boldsymbol{x}}^{\text{nl}}}$, the derivative $\partial \tilde{\boldsymbol{f}}_{\text{nl,red}} / \partial \tilde{\boldsymbol{x}}^{\text{nl}}$ must be evaluated. The chain rule and the use of the AFT matrix $\boldsymbol{\Gamma}^{-1}$ and $\boldsymbol{\Gamma}$ yield the expression:

$$\frac{\partial \tilde{\boldsymbol{f}}_{\text{nl,red}}}{\partial \tilde{\boldsymbol{x}}} = \boldsymbol{\Gamma}^{-1} \frac{\partial \boldsymbol{f}_{\text{nl,red}}}{\partial \boldsymbol{x}} \boldsymbol{\Gamma} + \boldsymbol{\Gamma}^{-1} \frac{\partial \boldsymbol{f}_{\text{nl,red}}}{\partial \dot{\boldsymbol{x}}} \boldsymbol{\Gamma} \left(\omega \boldsymbol{\nabla} \otimes \mathbf{I}_q\right) \tag{22}$$

The Jacobians of the time variable $\boldsymbol{f}_{\text{nl,red}}$ with respect to $\boldsymbol{x}$ and $\dot{\boldsymbol{x}}$, respectively denoted $\dfrac{\partial \boldsymbol{f}_{\text{nl,red}}}{\partial \boldsymbol{x}}$ and $\dfrac{\partial \boldsymbol{f}_{\text{nl,red}}}{\partial \dot{\boldsymbol{x}}}$, are calculated analytically.

The derivative with respect to ω that appears in (15) is computed as follows:

$$\mathbf{R}_{,\omega}\left(\mathbf{X}_i^k\right) = \frac{\partial \mathbf{R}}{\partial \omega}\left(\mathbf{X}_i^k\right) = \mathbf{Z}_{\text{red},\omega}(\omega) + \frac{\partial \tilde{\boldsymbol{f}}_{\text{nl,red}}}{\partial \omega}\left(\mathbf{X}_i^k\right) - \frac{\partial \tilde{\boldsymbol{f}}_{\text{ext,red}}}{\partial \omega}\left(\mathbf{X}_i^k\right) \tag{23}$$

3 Bifurcation tracking

The bifurcation tracking methodology for LP is presented in this section. First, in the subsection 3.1, the initial algebraic system resulting from the HBM is augmented in order to characterize the LP. Then, in the section 3.2, the continuation procedure which will make it possible to track LP is detailed.

3.1 Characterization of bifurcation points

For a given solution $\mathbf{X} = \left[\tilde{\boldsymbol{x}}^{\text{nl}}, \omega\right]^\top$, the condition $\mathbf{R}(\tilde{\boldsymbol{x}}^{\text{nl}}, \omega) = \mathbf{0}_{q_H}$ is met. This solution is regular if the Jacobian of the augmented system $\mathbf{R}_{,\mathbf{X}}$ verifies: $\text{rank}(\mathbf{R}_{,\mathbf{X}}) = n_{\text{eq}}$. Should this condition not be verified, the solution is said singular and corresponds to a bifurcation point. In particular, the identification of limit point relies on the following test function:

$$\tau_{LP}^1 = \det(\mathbf{R}_{,\tilde{\boldsymbol{x}}^{\text{nl}}}) \quad \text{for} \quad \boldsymbol{R}_{,\omega}^\top \boldsymbol{\phi} \neq 0 \tag{24}$$

The Jacobian matrix $\mathbf{R}_{,\tilde{\boldsymbol{x}}^{\text{nl}}}$ is therefore deficient of rank 1 and admits a zero eigenvalue associated with an eigenvector noted $\boldsymbol{\phi}$. Because the computation of $\det(\mathbf{R}_{,\tilde{\boldsymbol{x}}^{\text{nl}}})$ may be numerically challenging for high-dimensional systems,

several alternative techniques have been developed [21, 23, 25]. In this paper, the selected method [21, 25] consists in augmenting the system of equations such that:

$$\mathcal{R}(\mathbf{y}) = \begin{pmatrix} \mathbf{R}(\tilde{\boldsymbol{x}}^{\mathrm{nl}}, \omega) \\ \mathbf{R}_{,\tilde{\boldsymbol{x}}^{\mathrm{nl}}}\left(\tilde{\boldsymbol{x}}^{\mathrm{nl}}, \omega\right)\boldsymbol{\phi} \\ \boldsymbol{\phi}^{\top}\boldsymbol{\phi} - 1 \end{pmatrix} = \mathbf{0}_{2q_H+1} \tag{25}$$

where the first equation relates to the equilibrium of the system, the second equation characterizes the limit point and the last one normalizes the eigenvector ϕ. The unknown vector of the augmented system (25) is:

$$\mathbf{y} = \begin{pmatrix} \tilde{\boldsymbol{x}}^{\mathrm{nl}} \\ \boldsymbol{\phi} \\ \omega \end{pmatrix} \tag{26}$$

The solution vector $\boldsymbol{\phi}$ at the limit point is the eigenvector associated with the zero eigenvalue of the Jacobian matrix. While this formulation significantly increases the dimension of the system, its solution is less prone to numerical instabilities.

System (25) is solved by means of a nonlinear Newton-Raphson solver:

$$\mathbf{y}_i^{k+1} = \mathbf{y}_i^k + \Delta\mathbf{y}_i^k \quad \text{and} \quad \mathcal{R}^k_{,\mathbf{y}}\Delta\mathbf{y}^k = -\mathcal{R}^k \tag{27}$$

with

$$\mathcal{R}^k = \mathcal{R}\left(\mathbf{y}^k\right) \quad \text{and} \quad \mathcal{R}^k_{,\mathbf{y}} = \mathcal{R}_{,\mathbf{y}}(\mathbf{y}^k) = \frac{\partial\mathcal{R}(\mathbf{y}^k)}{\partial\mathbf{y}} \tag{28}$$

The convergence of the procedure is closely related to the accuracy of $\mathcal{R}_{,\mathbf{y}}(\mathbf{y})$:

$$\mathcal{R}_{,\mathbf{y}}(\mathbf{y}) = \begin{bmatrix} \mathbf{R}_{,\tilde{\boldsymbol{x}}^{\mathrm{nl}}} & \mathbf{0}_{q_H,q_H} & \mathbf{R}_{,\omega} \\ \left(\mathbf{R}_{,\tilde{\boldsymbol{x}}^{\mathrm{nl}}}\boldsymbol{\phi}\right)_{,\tilde{\boldsymbol{x}}^{\mathrm{nl}}} & \mathbf{R}_{,\tilde{\boldsymbol{x}}^{\mathrm{nl}}} & \left(\mathbf{R}_{,\tilde{\boldsymbol{x}}^{\mathrm{nl}}}\boldsymbol{\phi}\right)_{,\omega} \\ \mathbf{0}_{q_H}{}^{\top} & 2\boldsymbol{\phi} & 0 \end{bmatrix} \tag{29}$$

Both $\mathbf{R}_{,\tilde{\boldsymbol{x}}^{\mathrm{nl}}}$ and $\mathbf{R}_{,\omega}$ are already knwon since they are required for the calculation of the NFRC. Additional terms to compute are limited to: $\left(\mathbf{R}_{,\tilde{\boldsymbol{x}}^{\mathrm{nl}}}\boldsymbol{\phi}\right)_{,\tilde{\boldsymbol{x}}^{\mathrm{nl}}}$ and $\left(\mathbf{R}_{,\tilde{\boldsymbol{x}}^{\mathrm{nl}}}\boldsymbol{\phi}\right)_{,\omega}$.

$\left(\mathbf{R}_{,\tilde{\boldsymbol{x}}^{\mathrm{nl}}}\boldsymbol{\phi}\right)_{,\tilde{\boldsymbol{x}}^{\mathrm{nl}}}$ is here computed by finite differences:

$$\left(\mathbf{R}_{,\tilde{\boldsymbol{x}}^{\mathrm{nl}}}\boldsymbol{\phi}\right)_{,\tilde{\boldsymbol{x}}^{\mathrm{nl}}} \simeq \frac{1}{\epsilon_{\tilde{\boldsymbol{x}}^{\mathrm{nl}}}}\left[\mathbf{R}_{,\tilde{\boldsymbol{x}}^{\mathrm{nl}}}\left(\tilde{\boldsymbol{x}}^{\mathrm{nl}} + \epsilon_{\tilde{\boldsymbol{x}}^{\mathrm{nl}}}\phi\right) - \mathbf{R}_{,\tilde{\boldsymbol{x}}^{\mathrm{nl}}}\left(\tilde{\boldsymbol{x}}^{\mathrm{nl}}\right)\right] \tag{30}$$

with $\epsilon_{\tilde{\boldsymbol{x}}^{\mathrm{nl}}} = \eta\left(\dfrac{\|\tilde{\boldsymbol{x}}^{\mathrm{nl}}\|}{\|\phi\|} + \eta\right)$ and $\eta = 10^{-6}$.

$\left(\mathbf{R}_{,\tilde{\boldsymbol{x}}^{\mathrm{nl}}}\boldsymbol{\phi}\right)_{,\omega}$ is also computed by finite differences. As $\boldsymbol{\phi}$ is independent of ω, we can extract $\boldsymbol{\phi}$ from the derivative: $\left(\mathbf{R}_{,\tilde{\boldsymbol{x}}^{\mathrm{nl}}}\boldsymbol{\phi}\right)_{,\omega} = \mathbf{R}_{,\tilde{\boldsymbol{x}}^{\mathrm{nl}},\omega}\boldsymbol{\phi}$ with, by finite differences:

$$\mathbf{R}_{,\tilde{\boldsymbol{x}}^{\mathrm{nl}},\omega} \simeq \frac{1}{\epsilon_\omega}\left[\mathbf{R}_{,\tilde{\boldsymbol{x}}^{\mathrm{nl}}}\left(\omega + \epsilon_\omega\right) - \mathbf{R}_{,\tilde{\boldsymbol{x}}^{\mathrm{nl}}}\left(\omega\right)\right] \tag{31}$$

with $\epsilon_\omega = \eta\left(\|\omega\| + \eta\right)$ and $\eta = 10^{-6}$. $\mathbf{R}_{,\tilde{\boldsymbol{x}}^{\mathrm{nl}},\omega}$ can also be obtained by deriving the expression of the Jacobian $\mathbf{R}_{,\tilde{\boldsymbol{x}}^{\mathrm{nl}}}$ with respect to ω:

$$\mathbf{R}_{,\tilde{\boldsymbol{x}}^{\mathrm{nl}},\omega} = \boldsymbol{Z}_{\mathrm{red},\omega} + \frac{\partial^2\tilde{\boldsymbol{f}}_{\mathrm{nl,red}}}{\partial\tilde{\boldsymbol{x}}^{\mathrm{nl}}\partial\omega} \tag{32}$$

3.2 Continuation of bifurcation points

At this stage, limit points are found in the parametric space $(\tilde{\boldsymbol{x}}^{\mathrm{nl}}, \omega)$. In order to assess the location of limit points as any given parameter of the system—denoted γ in this section—varies, the numerical strategy is augmented with an arc-length continuation technique. The vector of unknowns $\mathbf{Y}$ now includes γ:

$$\mathbf{Y} = \begin{pmatrix} \tilde{\boldsymbol{x}}^{\mathrm{nl}} \\ \boldsymbol{\phi} \\ \omega \\ \gamma \end{pmatrix} \tag{33}$$

3.2.1 Prediction

An initial guess $\mathbf{Y}_i^0$ is required to compute the solution $\mathbf{Y}_i$. For $i \geq 2$, the prediction of the solution i is calculated with secant prediction from the converged solutions $i-1$ and $i-2$:

$$\mathbf{Y}_i^0 = \mathbf{Y}_{i-1} + \delta s \frac{\Delta \mathbf{Y}_{i-1}}{\|\Delta \mathbf{Y}_{i-1}\|} \text{ with } \Delta \mathbf{Y}_{i-1} = \mathbf{Y}_{i-1} - \mathbf{Y}_{i-2} \tag{34}$$

The prediction $\mathbf{Y}_0^0 = \left[\tilde{\boldsymbol{x}}_0^{0,\mathrm{nl}}, \boldsymbol{\phi}_0^0, \omega_0^0, \gamma_0^0\right]^\top$ is constructed from a NFRC. Consider a NFRC computed in the plane $\left(\tilde{\boldsymbol{x}}^{\mathrm{nl}}, \omega\right)$ for a given parameter space with γ^*. The second control parameter is therefore chosen such as $\gamma_0^0 = \gamma^*$. As described above, a limit point can be detected using test functions and the associated $\mathbf{X}_0^0 = \left[\tilde{\boldsymbol{x}}_0^{0,\mathrm{nl}}, \omega_0^0\right]^\top$ is obtained. Finally, the eigenvector $\boldsymbol{\phi}_0^0$ is chosen as the eigenvector $\phi_{\min}$ associated with the eigenvalue having the lowest absolute value: $\boldsymbol{\phi}_0^0 = \phi_{\min}$.

For $\mathbf{Y}_1$, the prediction $\mathbf{Y}_1^0$ is chosen identical to $\mathbf{Y}_0$ with a slight shift of the second control parameter γ: $\mathbf{Y}_1^0 = \left[\tilde{\boldsymbol{x}}_0^{0,\mathrm{nl}}, \boldsymbol{\phi}_0^0, \omega_0^0, \gamma_0^0 + \delta\gamma\right]^\top$.

3.2.2 Parameterization

Given the second control parameter γ, the dimension of the nonlinear algebraic system (25) is increased by one. The nonlinear augmented algebraic system $\mathcal{S}(\mathbf{Y})$ now consists of $2q_H + 2$ equations:

$$\mathcal{S}(\mathbf{Y}) = \begin{pmatrix} \mathbf{R}(\tilde{\boldsymbol{x}}^{\mathrm{nl}}, \omega) \\ \mathbf{R}_{,\tilde{\boldsymbol{x}}^{\mathrm{nl}}}\left(\tilde{\boldsymbol{x}}^{\mathrm{nl}}, \omega\right) \boldsymbol{\phi} \\ \boldsymbol{\phi}^\top \boldsymbol{\phi} - 1 \\ \mathcal{P}(\tilde{\boldsymbol{x}}^{\mathrm{nl}}, \boldsymbol{\phi}, \omega, \gamma, s) \end{pmatrix} = \mathbf{0}_{2q_H+2} \tag{35}$$

The arc-length continuation procedure, presented in the section 2.2.2, leads to:

$$\begin{aligned} \mathcal{P}\left(\mathbf{Y}_i^k, s\right) = &\left\|\tilde{\boldsymbol{x}}_i^{k,\mathrm{nl}} - \tilde{\boldsymbol{x}}_{i-1}^{\mathrm{nl}}\right\|^2 + \left\|\boldsymbol{\phi}_i^k - \boldsymbol{\phi}_{i-1}\right\|^2 \\ &+ \left(\omega_i^k - \omega_{i-1}\right)^2 + \left(\gamma_i^k - \gamma_{i-1}\right)^2 - \delta s^2 = 0 \end{aligned} \tag{36}$$

Iterates $\mathbf{Y}_i^k$ are therefore located on the hypersphere $\mathbb{R}^{2q_H+2}$ of radius δs centered in $\mathbf{Y}_{i-1}$. Thus, the converged solution $\mathbf{Y_i}$ is located at the intersection of the curve $\mathcal{S}\left(\mathbf{Y}_i^k\right) = \mathbf{0}_{2q_H+2}$ and the hypersphere $\mathbb{R}^{2q_H+2}$ of radius δs centered at $\mathbf{Y}_{i-1}$.

3.2.3 Correction

The algebraic system (35) is solved using the iterative Newton-Raphson procedure (37).

$$\mathbf{Y}_i^{k+1} = \mathbf{Y}_i^k + \Delta \mathbf{Y}_i^k \quad \text{with} \quad \mathcal{S}_{,\mathbf{Y}}^k \Delta \mathbf{Y}_i^k = -\mathcal{S}^k \tag{37}$$

with

$$\mathcal{S}^k = \mathcal{S}\left(\mathbf{Y}_i^k\right) \quad \text{and} \quad \mathcal{S}^k_{,\mathbf{Y}} = \mathcal{S}_{,\mathbf{Y}}(\mathbf{Y}_i^k) = \frac{\partial \mathcal{S}(\mathbf{Y}_i^k)}{\partial \mathbf{Y}} \tag{38}$$

$\mathbf{Y}_i^{k+1}$ is therefore calculated as: $\mathbf{Y}_i^{k+1} = \mathbf{Y}_i^k + \delta\mathbf{Y}_i^k$. The prediction $\mathbf{Y}_i^{k=0}$ obtained by the secant method allows to initialize the Newton-Raphson algorithm correctly.

The Jacobian matrix of the augmented system $\mathcal{S}_{,\mathbf{Y}}(\mathbf{Y})$ is expressed as follows:

$$\mathcal{S}_{,\mathbf{Y}}(\mathbf{Y}) = \begin{bmatrix} \mathbf{R}_{,\tilde{\boldsymbol{x}}^{\mathrm{nl}}} & \mathbf{0}_{q_H,q_H} & \mathbf{R}_{,\omega} & \mathbf{R}_{,\gamma} \\ \left(\mathbf{R}_{,\tilde{\boldsymbol{x}}^{\mathrm{nl}}}\boldsymbol{\phi}\right)_{,\tilde{\boldsymbol{x}}^{\mathrm{nl}}} & \mathbf{R}_{,\tilde{\boldsymbol{x}}^{\mathrm{nl}}} & \left(\mathbf{R}_{,\tilde{\boldsymbol{x}}^{\mathrm{nl}}}\boldsymbol{\phi}\right)_{,\omega} & \left(\mathbf{R}_{,\tilde{\boldsymbol{x}}^{\mathrm{nl}}}\boldsymbol{\phi}\right)_{,\gamma} \\ \mathbf{0}_{q_H}{}^{\top} & 2\boldsymbol{\phi}^{\top} & 0 & 0 \\ \mathcal{P}^{\top}_{,\tilde{\boldsymbol{x}}^{\mathrm{nl}}} & \mathcal{P}^{\top}_{,\boldsymbol{\phi}} & \mathcal{P}_{,\omega} & \mathcal{P}_{,\gamma} \end{bmatrix} \tag{39}$$

$\mathbf{R}_{,\gamma}\left(\mathbf{Y}_i^k\right)$ can be obtained by deriving the expression (9) of the residual $\mathbf{R}\left(\mathbf{Y}_i^k\right)$ with respect to γ:

$$\mathbf{R}_{,\gamma} = \mathbf{Z}_{\mathrm{red},\gamma}\tilde{\boldsymbol{x}}^{\mathrm{nl}} + \frac{\partial \tilde{\boldsymbol{f}}_{\mathrm{nl,red}}}{\partial\gamma} - \frac{\partial \tilde{\boldsymbol{f}}_{\mathrm{ext,red}}}{\partial\gamma} \tag{40}$$

or, through finite differences:

$$\mathbf{R}_{,\gamma} \simeq \frac{1}{\epsilon_\gamma}\left[\mathbf{R}\left(\gamma+\epsilon_\gamma\right) - \mathbf{R}\left(\gamma\right)\right] \tag{41}$$

with $\epsilon_\gamma = \eta\left(\|\gamma\| + \eta\right)$ and $\eta = 10^{-6}$.

As $\boldsymbol{\phi}$ is independent of γ, $\boldsymbol{\phi}$ may be obtained from the derivative: $\left(\mathbf{R}_{,\tilde{\boldsymbol{x}}^{\mathrm{nl}}}\boldsymbol{\phi}\right)_{,\gamma} = \mathbf{R}_{,\tilde{\boldsymbol{x}}^{\mathrm{nl}},\gamma}\boldsymbol{\phi}$. $\mathbf{R}_{,\tilde{\boldsymbol{x}}^{\mathrm{nl}},\gamma}$ is obtained by deriving the expression of the Jacobian $\mathbf{R}_{,\tilde{\boldsymbol{x}}^{\mathrm{nl}}}\left(\mathbf{Y}_i^k\right)$ with respect to γ:

$$\mathbf{R}_{,\tilde{\boldsymbol{x}}^{\mathrm{nl}},\gamma} = \boldsymbol{Z}_{\mathrm{red},\gamma} + \frac{\partial^2 \tilde{\boldsymbol{f}}_{\mathrm{nl,red}}}{\partial\tilde{\boldsymbol{x}}^{\mathrm{nl}}\partial\gamma} \tag{42}$$

or, by finite differences:

$$\mathbf{R}_{,\tilde{\boldsymbol{x}}^{\mathrm{nl}},\gamma} \simeq \frac{1}{\epsilon_\gamma}\left[\mathbf{R}_{,\tilde{\boldsymbol{x}}^{\mathrm{nl}}}\left(\gamma+\epsilon_\gamma\right) - \mathbf{R}_{,\tilde{\boldsymbol{x}}^{\mathrm{nl}}}\left(\gamma\right)\right] \tag{43}$$

Derivatives of $\mathcal{P}$ are:

$$\begin{cases} \dfrac{\partial\mathcal{P}\left(\mathbf{Y}_i^k\right)}{\partial\tilde{\boldsymbol{x}}^{\mathrm{nl}}}^{\top} &= 2\left(\tilde{\boldsymbol{x}}_i^{k,\mathrm{nl}} - \tilde{\boldsymbol{x}}_{i-1}^{\mathrm{nl}}\right) \\ \dfrac{\partial\mathcal{P}\left(\mathbf{Y}_i^k\right)}{\partial\boldsymbol{\phi}}^{\top} &= 2\left(\boldsymbol{\phi}_i^k - \boldsymbol{\phi}_{i-1}\right) \\ \dfrac{\partial\mathcal{P}\left(\mathbf{Y}_i^k\right)}{\partial\omega} &= 2\left(\omega_i^k - \omega_{i-1}\right) \\ \dfrac{\partial\mathcal{P}\left(\mathbf{Y}_i^k\right)}{\partial\gamma} &= 2\left(\gamma_i^k - \gamma_{i-1}\right) \end{cases} \tag{44}$$

The condition:

$$\left\|\mathcal{S}\left(\mathbf{Y}_i^k\right)\right\| \leq \epsilon \tag{45}$$

is used to end the iterative process where ϵ is dependent on the system of interest.

Figure 1. NASA rotor 67: (a) full blade disk [33], (b) finite element mesh with boundary nodes (●) [34]

4 Blade-tip/casing interactions on NASA Rotor 67

In this paper, the proposed numerical strategy is implemented for the nonlinear analysis of NASA rotor 67 [32], clamped at its root, as it undergoes structural contacts along its tip, see Fig.1. This open blade model has already been used as a case study in various fields of research [6, 8, 15]. The blade mechanical model and the considered contact scenario presented below are identical to those of the article [16] for the sake of consistency.

4.1 Blade model

The blade material is a titanium alloy of grade 5, TA6V (Ti 6Al 4V). Its properties are given in Tab.1. The CAD

Young's modulus E	Density ρ	Poisson's ratio ν
108 GPa	4400 kg·m^{-3}	0.34

Table 1. Material properties

model of the blade is meshed with 129181 quadratic pentahedron elements. The finite element mesh is shown in Fig.1b. The Craig-Bampton model reduction procedure [35, 36] is used in order to generate a reduced-order model: $n_\mathrm{b} = 9$ boundary nodes are retained along the blade-tip (see,(●) in Fig.1b) along with $\eta = 12$ fixed-interface modes. The reduced model is therefore composed of $q_H = 39$ dof. A modal damping coefficient $\xi_{1-2} = 1 \cdot 10^{-3}$ is considered for the first two bending modes (1B and 2B), $\xi_{3+} = 5 \cdot 10^{-3}$ for all other modes. The three first eigenfrequencies of the blade are provided in Tab. 2.

Mode	1B	2B	1T
ω [rad·s^{-1}]	2039.78	6343.69	10745.26
f [Hz]	324.640	1009.63	1710.16

Table 2. Eigenfrequencies of the first three modes

4.2 Contact scenario

The casing surrounding the bladed disk is assumed perfectly rigid, it is modelled by a cylindrical envelope. Operating clearances, denoted c_j in Fig.2, correspond to the distance between a boundary node (●) and the casing (⊸). They are here considered constant at rest: for each of the n_b boundary nodes, $c_j = 4 \cdot 10^{-4}$ m. In order to initiate contact between the blade tip and the casing, the blade is excited along the first harmonics of its first bending mode

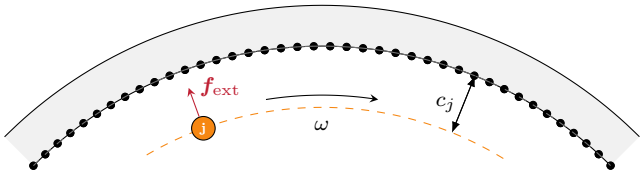

Figure 2. Blade-tip/casing modelling [17]

with a dimensionless amplitude A.

$$\boldsymbol{f}_{\text{ext}}\left(\omega,t\right) = AM\phi_{1\text{F}}\cos\left(\omega t\right) \tag{46}$$

Contact forces $\boldsymbol{f}_{\text{nl}}^{\text{N}}$ are calculated from the gap function $\boldsymbol{g}(t) = \boldsymbol{x}(t) - c_j$ using a polynomial contact regularization law. In addition, a Lanczos filtering is applied in order to attenuate the Gibbs phenomenon [15].

As the blade is in contact with the casing, dry friction forces, respectively circumferential (47) and axial (48), are calculated for the j-th boundary node at time t_i. Permanent sliding is assumed given the high relative velocities involved.

$$\boldsymbol{f}_{\text{nl},j}^{\theta}\left(t_i\right) = \mu\frac{v_j^{\theta}\left(t_i\right) + \rho_j\omega}{\sqrt{\left(v_j^{\theta}\left(t_i\right) + \rho_j\omega\right)^2 + v_j^{z}\left(t_i\right)^2}}\boldsymbol{f}_{\text{nl},j}^{\text{N}}\left(t_i\right) \tag{47}$$

$$\boldsymbol{f}_{\text{nl},j}^{z}\left(t_i\right) = \mu\frac{v_j^{z}\left(t_i\right)}{\sqrt{\left(v_j^{\theta}\left(t_i\right) + \rho_j\omega\right)^2 + v_j^{z}\left(t_i\right)^2}}\boldsymbol{f}_{\text{nl},j}^{\text{N}}\left(t_i\right) \tag{48}$$

where $\mu = 0.15$ is the dry friction coefficient, v_j^{θ} and v_j^{z}, the circumferential and axial velocities and ρ_j, the radial distance of the j-th boundary node from of the axis of rotation.

5 Numerical results

The bifurcation tracking methodology presented in section 3 is implemented numerically in Python 3. From an initial NFRC calculated by RL-HBM, the tracking of detected limit points is carried out considering variations of the following key parameters: the dimensionless amplitude A, the friction coefficient μ and the operating clearances c_j.

5.1 Nonlinear Frequency Response Curve

Computations are first run for $A = 140$, $\mu = 0.15$ and $c_j = 4 \cdot 10^{-4}$ m (—). RL-HBM numerical parameters are as follows: $H = 10$ harmonics and $N = 2^{10}$ time instants are considered. The NFRC obtained for the leading and the trailing edges (—) are depicted in Fig. 3. A stability analysis is conducted to determine the stability of solution branches and detect the limit points. Solid lines correspond to stable branches of solutions whereas dashed lines correspond to unstable branches of solutions resulting from Floquet framework stability analysis [19]. In total, four limit points (●) are detected and denoted LP_i in Fig. 3.

Over a period T, the time signals of the displacements $||\mathbf{r}_i(t)||_\infty$ and the nonlinear forces $||\mathbf{f}_{nl,i}(t)||_\infty$ at the nonlinear resonance (LP3) are depicted in Fig. 4. The signals at the leading edge are in solid line while those at the trailing edge are in dashed line. A very good agreement between the displacements obtained by time integration (—) and by RL-HBM (—) can be observed. The maximum reached by the displacement signal $||\mathbf{r}_1(t)||_\infty$ is -1.42 mm and by $||\mathbf{r}_9(t)||_\infty$ -0.89mm which is in agreement with the values obtained by the NFRC in Fig. 3. In order to better illustrate the relevance of the value of H and N, the Fourier coefficients of the nonlinear resonance solution (LP3) are depicted in Fig. 5. This histogram indicates that main contributions relate to the harmonics a_0, a_1, b_1, a_2 and b_2. For this particular solution, contributions of harmonics higher than 6 are found negligible.

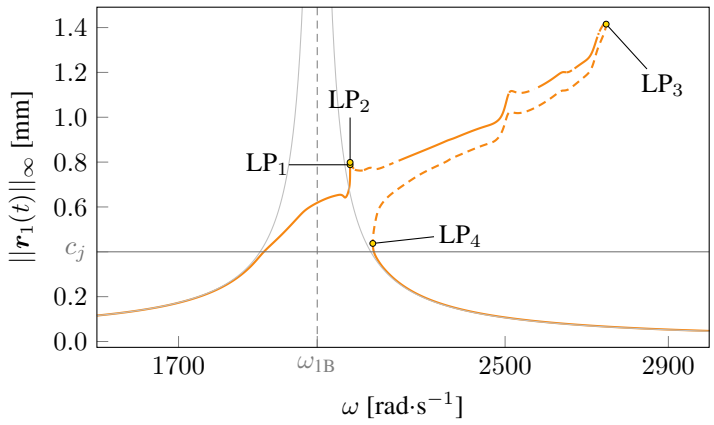

(a) Leading edge

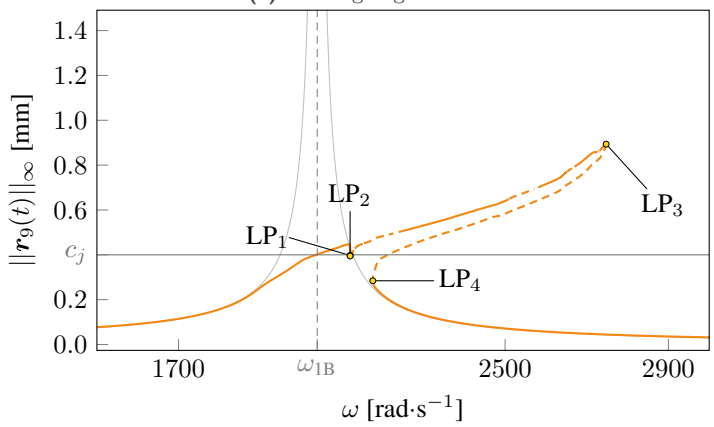

(b) Trailing edge

Figure 3. Rotor 67 leading and trailing edges nonlinear frequency response curves (—) with LP (●) for $A = 140$, $\mu = 0.15$ and $c_j = 4 \cdot 10^{-4}$ m

5.2 Bifurcation tracking

The limit points detected on the NFRC (Fig. 3) are tracked according to the three aforementioned control parameters: the dimensionless amplitude A, the friction coefficient μ and operating clearances c_j.

5.2.1 Dimensionless amplitude A

The bifurcation tracking of LP$_2$/LP$_3$ (—) and LP$_1$/LP$_4$ (—) are depicted in Fig. 6. Figure 6. shows that the bifurcation tracking curve of LP$_2$ is the same as that of LP$_3$ and that of LP$_1$ is the same as that of LP$_4$.

In order to validate the results obtained by bifurcation tracking, several NFRC (—) are calculated for different values of A: $A \in [20, 40, 60, 80, 100, 120]$, depicted in Fig.6. Such a large interval is considered to simulate contact events of distinct levels of severity. A comparison between the results of the bifurcation tracking and the bifurcations detected on the NFRC underlines that curves (—) and (—) pass through the predicted bifurcation points (●).

Looking at the NFRC (—) obtained for each value of A, a discontinuity between the main NFRC for $A = 40$ and that for $A = 60$ can be observed. For $A = 20$ and $A = 40$, isolated branches of solutions seem not to have been calculated. Indeed, the initialization made for the calculation of the main NFRC does not make it possible to reach isolated branches of solutions. To compute them, it is therefore necessary to initialize the procedure for calculating an NFRC with a point close to this isolated branch of solutions. For that, a point of the bifurcation tracking curve (—) close to this isolated branch of solutions is taken. The calculated isolated branches of solutions (—) are

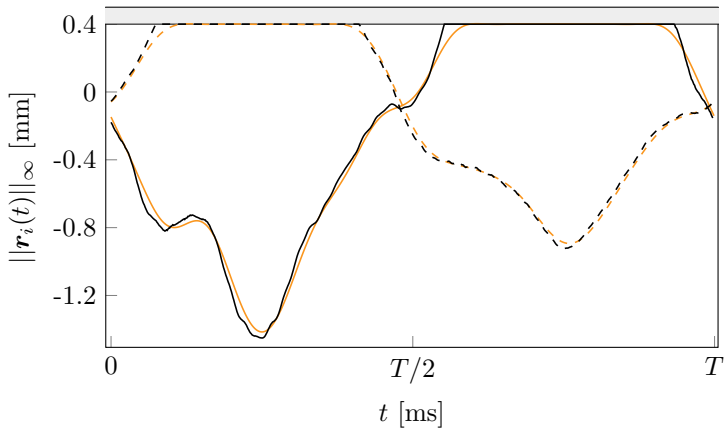

(a) Displacements

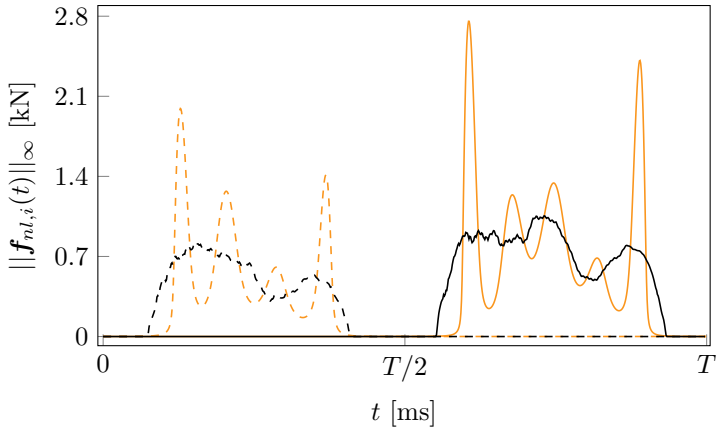

(b) Nonlinear forces

Figure 4. Time signals of the dispacements and the nonlinear forces obtained at LP_3 by time integration (— / - -) and by RL-HBM (— / - -)

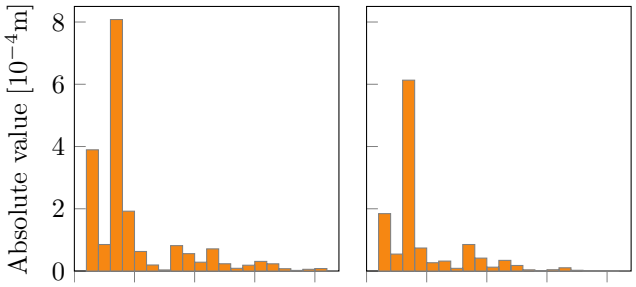

Figure 5. Fourier coefficients (a_0, a_1, b_1, …, a_H, b_H) of $||\mathbf{r}_1(t)||_\infty$ (left) and $||\mathbf{r}_9(t)||_\infty$ (right) at LP_3

shown in Fig. 6. Again, a comparison between the results of the bifurcation tracking and the bifurcations detected on the isolated branches of solutions underlines that curves (—) and (—) pass through the predicted bifurcation points (●).

Bifurcation tracking curves in Fig. 6 are projected onto the plane (ω, A), see Fig. 7. As A increases, a local minimum on this curve corresponds to the appearance of isolated branches of solutions (▼). To the contrary, local

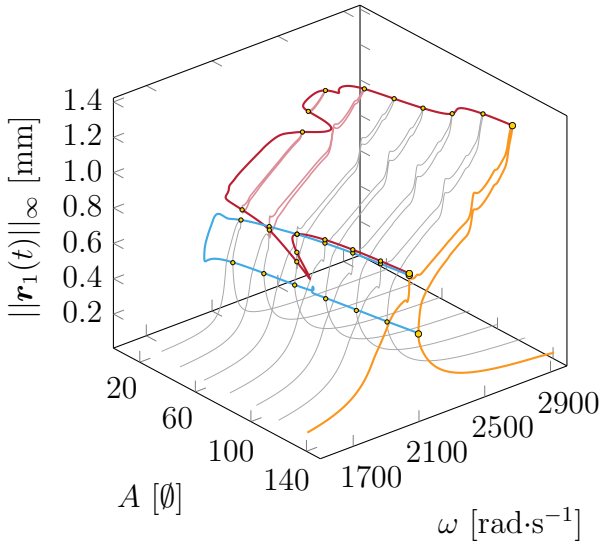

(a) Leading edge

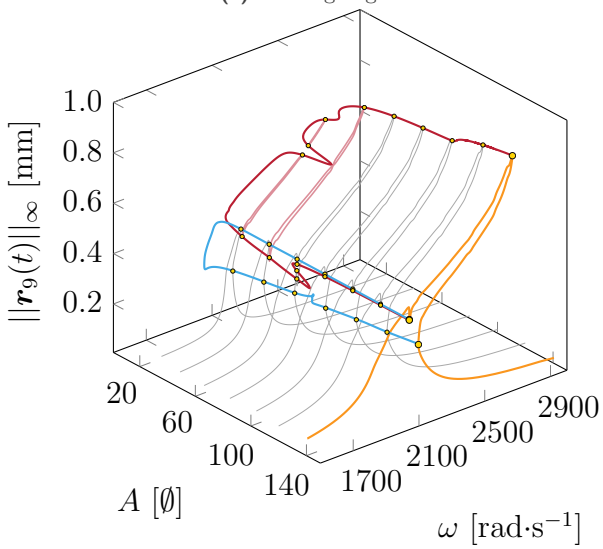

(b) Trailing edge

Figure 6. Rotor 67 leading and trailing edges bifurcation tracking (—/—) between $A = 20$ and $A = 140$ with isolated branches of solutions (—)

maxima correspond to areas where isolated branches of solutions merge between themselves or with the main NFRC (△). Figure 7 underscores the existence of five families of isolated branches of solutions, denoted $\mathcal{I}_i$.

For low values of A, the parameters for which three isolated branches of solutions ($\mathcal{I}_1, \mathcal{I}_2, \mathcal{I}_3$) appear are listed in Tab. 3. As A increases, these isolated branches of solutions will progressively merge into larger branches of solutions for the parameters listed in Tab. 4. Finally, for $A \geq 56.69$, no isolated branch of solutions is predicted anymore.

These results highlight the potential of bifurcation tracking for structural design purposes. Bifurcation tracking makes it possible to detect isolated branches of solutions in a similar fashion to Melnikov principle-based approaches [17] but also makes it possible to know the exact points where these isolated branches of solutions may merge with the main NFRC. In addition, bifurcation tracking also brings further qualitative pieces of information

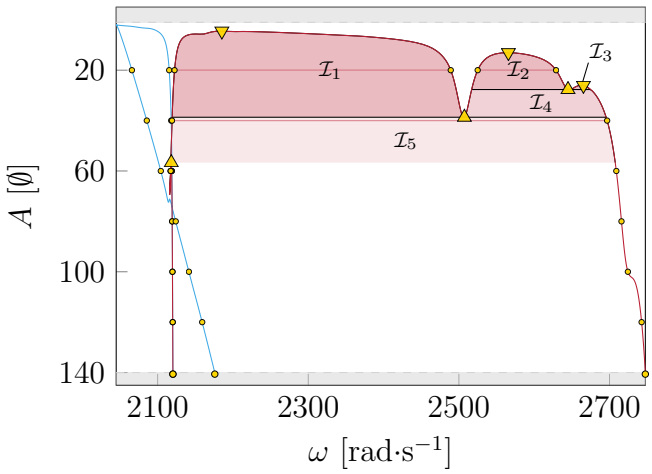

Figure 7. Projection of Fig 6. Bifurcation tracking curves in the plane (ω,A)

Appearance	ω [rad·s^{-1}]	A [∅]
$\mathcal{I}_1$	2185.31	4.49
$\mathcal{I}_2$	2565.77	13.03
$\mathcal{I}_3$	2665.37	26.03

Table 3. Appearance of isolated branches of solutions

Mergence	ω [rad·s^{-1}]	A [∅]
$\mathcal{I}_4 = \mathcal{I}_2 + \mathcal{I}_3$	2677.91	27.68
$\mathcal{I}_5 = \mathcal{I}_1 + \mathcal{I}_4$	2507.32	38.68
NFRC = NFRC + $\mathcal{I}_5$	2118.13	56.69

Table 4. Merging of isolated branches of solutions

with respect to the influence of A.

5.2.2 Friction coefficient μ

The bifurcation tracking of LP$_1$/LP$_2$ (—) and LP$_3$/LP$_4$ (—) as the friction coefficient μ varies are shown in Fig. 8. Figure 8 shows that the bifurcation tracking curve of LP$_1$ is the same as that of LP$_2$ and that of LP$_3$ is the same as that of LP$_4$. In order to validate the results obtained by bifurcation tracking, several NFRC (—) are calculated for different values of μ: $\mu \in [1 \cdot 10^{-4}, 0.025, 0.05, \ldots, 0.2]$, as depicted in Fig.8.

From $\mu \geq 0.2$, the selected numerical parameters no longer allow to compute the NFRC. It would probably be necesary to increase the number of harmonics ($H = 10$) to obtain accurate results for $\mu \geq 0.2$. While such results could be of interest from an academic standpoint, it goes beyond the scope of this article as typical friction coefficients in such blade-tip/casing contacts is usually less than 0.15. Nonetheless, even with $H = 10$, the bifurcation tracking of LP$_3$/LP$_4$ (—) was successful. Both very high vibration amplitudes and a complex shape of the bifurcation tracking curve underline the intricacy of vibration phenomena occuring for $\mu \geq 0.2$.

5.2.3 Operating clearances c_j

The bifurcation tracking of LP$_1$/LP$_2$ (—), LP$_3$ (—) and LP$_4$ (—) are shown in Fig. 9.

The bifurcation tracking of LP$_3$ is of particular interest. Indeed, the bifurcation tracking curve (—) turns around and returns to $c_j = 4 \cdot 10^{-4}$ m towards a LP which does not belong to the main NFRC. Additional RL-HBM

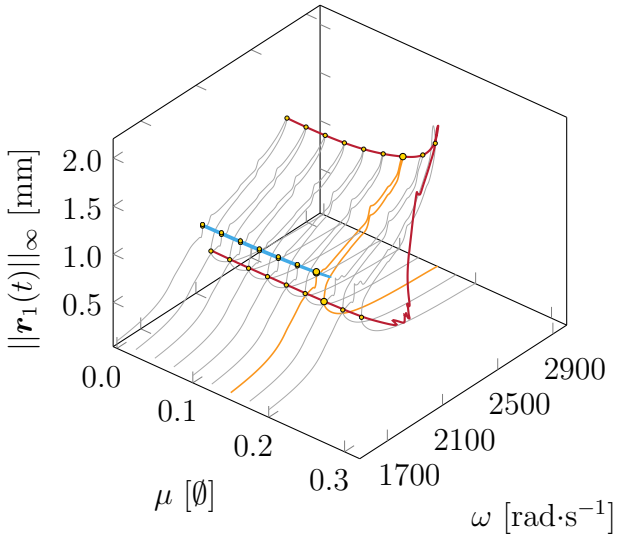

(a) Leading edge

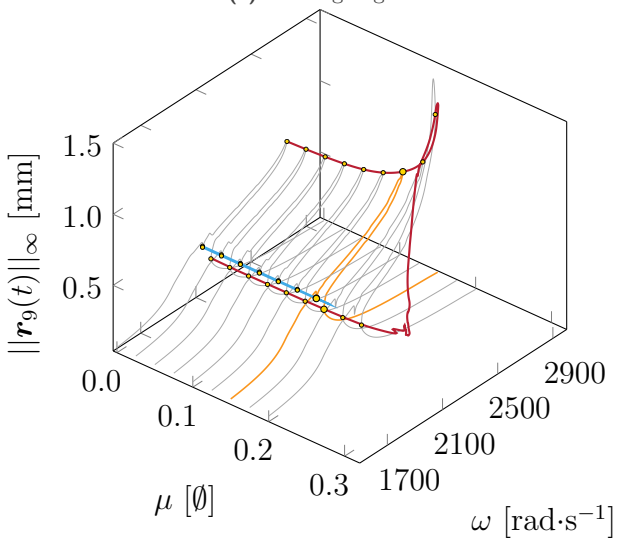

(b) Trailing edge

Figure 8. Rotor 67 leading and trailing edges bifurcation tracking (—/—) between $\mu = 0.3$ and $\mu = 0$

computations from this LP yields an isolated branch of solutions (—). The bifurcation tracking (- - -) of the second LP belonging to this isolated solution branch yields another LP belonging to a second isolated branch of solutions (—). In this particular configuration, bifurcation tracking with respect to the blade-tip/casing clearance thus yields isolated branches of solutions featuring very high vibration amplitudes that could not have been predicted otherwise.

In order to validate the results obtained by bifurcation tracking, several NFRC (—) and isolated branches of solutions (—) are calculated for different values of c_j: $c_j \in [1.0, 1.6, 2.2, 2.8, 3.4, 4.0] \cdot 10^{-4}$ m, depicted in Fig.9. By closely comparing the results of the bifurcation tracking against the bifurcations detected on the NFRCs, the bifurcation tracking curves pass through bifurcation points (●).

Looking at the projection of the bifurcation tracking curves onto the plane (ω, c_j), see Fig. 10, it is possible to observe more clearly the values of c_j for which isolated branches of solutions are predicted. Similarly to the analysis

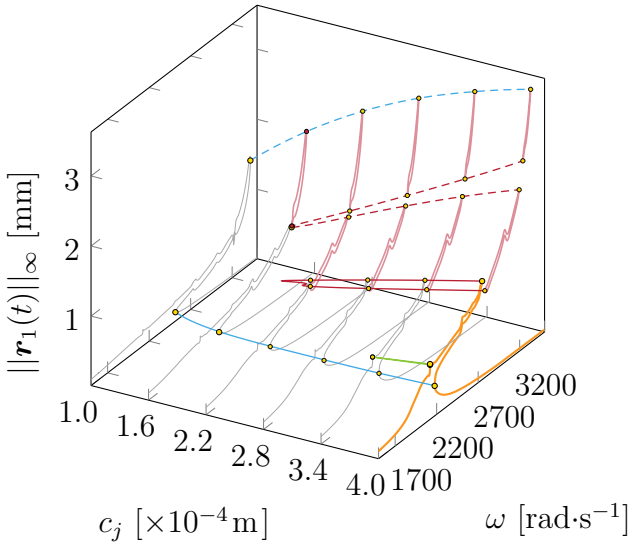

(a) Leading edge

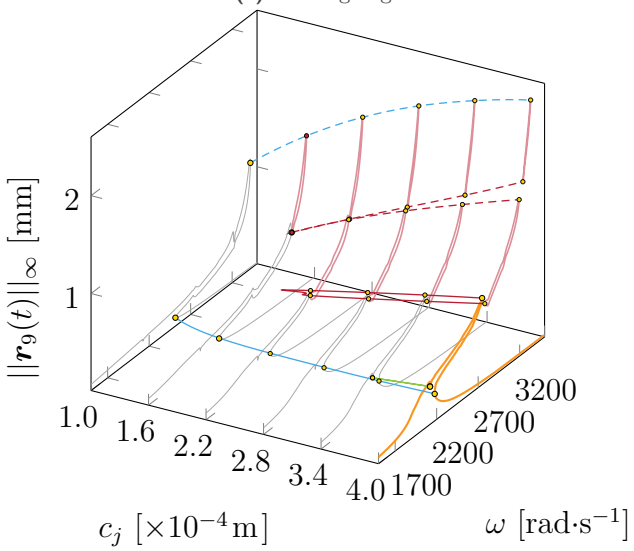

(b) Trailing edge

Figure 9. Rotor 67 leading and trailing edges bifurcation tracking (—/—/—/- - /- -) between $c_j = 1 \cdot 10^{-4}$ m and $c_j = 4 \cdot 10^{-4}$ m with isolated branches of solutions (—)

carried out above with respect to the dimensionless amplitude A, two areas—denoted $\mathcal{I}_1$ and $\mathcal{I}_2$—featuring isolated branches of solutions are evidenced.

These results underline the intricacy of the dynamics of NASA rotor 67 as it undergoes blade-tip/casing contacts. Should the analysis be limited to RL-HBM results, one may have the impression that vibration amplitudes at the nonlinear resonance decrease from $c_j = 0.4$ mm to $c_j = 0.22$ mm before a sudden increase is evidenced for lower values of c_j, see curves (—) and (—) in Fig. 11. However, thanks to the proposed bifurcation tracking strategy and the prediction of isolated branches of solutions, a very consistent decrease of the vibration amplitudes at the nonlinear resonance is observed as c_j decreases.

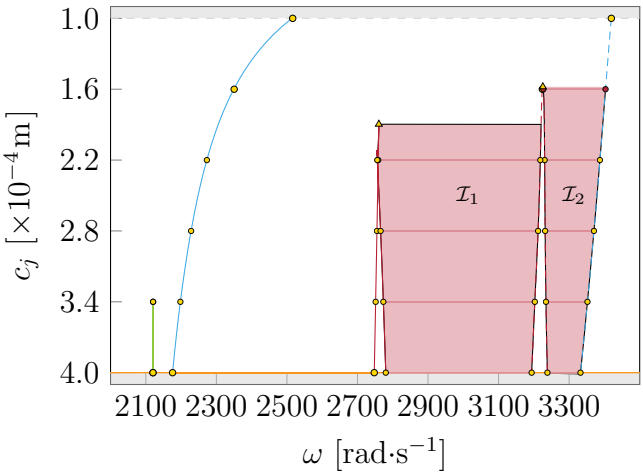

Figure 10. Projection of Fig. 9. Bifurcation tracking in the plane (ω, c_j)

5.3 Industrial benefit

Blade-tip/casing clearance has long been thought to be a key parameter for blade-tip/casing interactions. With the development of advanced numerical methodologies and the proposed bifurcation tracking approach, it is now possible to confirm that there are isolated branches of solutions with extreme vibration amplitudes that relate to this parameter. For the configuration of interest on NASA rotor 67, the proposed approach specifically yields two isolated branches of solutions whose relevance has been confirmed by direct comparison to time integration results, see Fig. 12. This observation corroborates recent findings [17] made using a distinct methodology on the same industrial model.

6 Conclusion

This paper addresses the issue of bifurcation tracking on high-dimensional industrial systems. It is shown that the regularized-Lanczos harmonic balance method is well-suited to the application of bifurcation tracking strategies. In particular, presented results underline the robustness of the proposed approach for the tracking of limit points for a variety of system parameters, thus providing original results on the influence of the friction coefficient, the forcing amplitude as well as operating blade-tip/casing clearances on the blade's dynamics. The possibility to build on the proposed approach to predict isolated branches of solutions is underlined in the article. Contrary to other

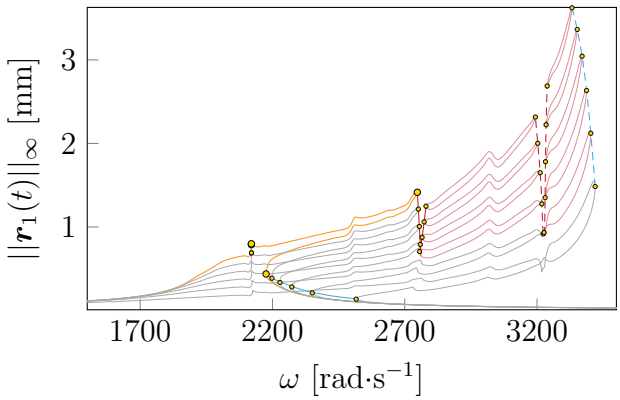

Figure 11. Projection of Fig. 9a in the plane $(\omega, ||r_1(t)||_\infty)$

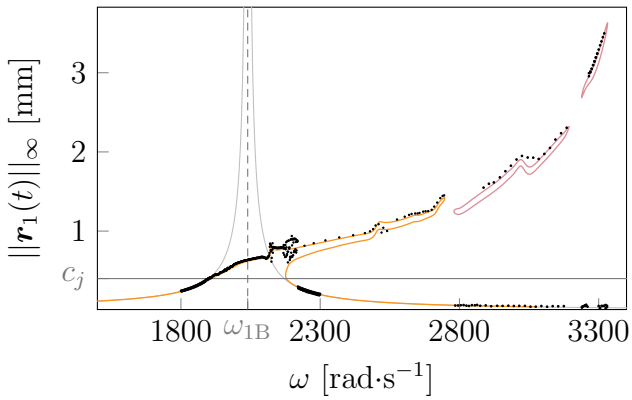

(a) Leading edge

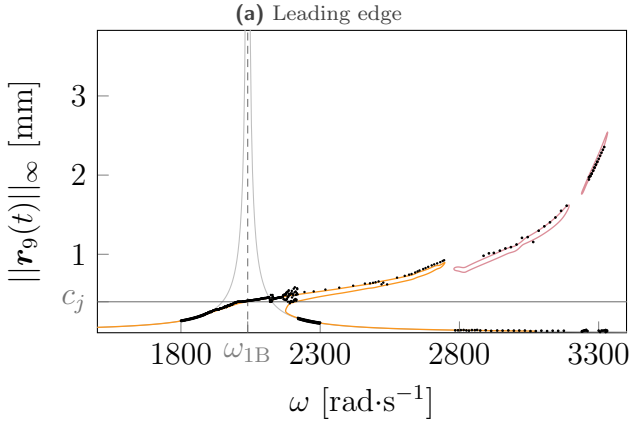

(b) Trailing edge

Figure 12. Rotor 67 blade leading and trailing edge nonlinear frequency response curves (—), isolated branches of solutions (—) and time integration results (•) for $A = 140$, $\mu = 0.15$ and $c_j = 4 \cdot 10^{-4}$ m

methodologies dedicated to isolated solution branches, the proposed approach advantageously allows to locate areas of the design space where isolated branches of solutions may appear.

Acknowledgments

This research was undertaken thanks to funding from the Canada Research Chairs Program. The authors would like to thank Thibaut Vadcard, Ph.D. student at Polytechnique Montréal and École Centrale de Lyon for his help in the implementation of the numerical developments presented in the article.

References

[1] S. Nacivet, C. Pierre, F. Thouverez, and L. Jezequel. A dynamic Lagrangian frequency–time method for the vibration of dry-friction-damped systems. Journal of Sound and Vibration Vol. 265, No. 1 (2003), 201–219. DOI: 10.1016/S0022-460X(02)01447-5.

[2] M. M. Gola. A general geometrical theory of turbine blade underplatform asymmetric dampers. Mechanical Systems and Signal Processing Vol. 191 (2023), 110167. DOI: 10.1016/j.ymssp.2023.110167.

[3] N. Maroldt, R. P.-v. S. L. R. R. W. J. Schwerdt L.. Berger, and J. R. Seume. Reduced Order Modeling of Forced Response in a Multistage Compressor Under Mistuning and Aerocoupling. Journal of Engineering for Gas Turbines and Power Vol. 144, No. 11 (2022). DOI: 10.1115/1.4055368.

[4] Y. B. Kim, S. T. Noah, and Y. S. Choi. Periodic response of multi-disk rotors with bearing clearances. Journal of Sound and Vibration Vol. 144, No. 3 (1991), 381–395. DOI: 10.1016/0022-460X(91)90558-2.

[5] J. Jiang. The analytical solution and the existence condition of dry friction backward whirl in rotor-to-stator contact systems. Journal of Vibration and Acoustics Vol. 129, No. 2 (2007), 260–264. DOI: 10.1115/1.2345677.

[6] A. J. Strazisar, J. R. Wood, M. D. Hathaway, and K. L. Suder. *Laser anemometer measurements in a transonic axial-flow fan rotor*. NASA Lewis Research Center Cleveland, OH, United States. 1989.

[7] C. Padova, J. Barton, M. Dunn, and S. Manwaring. Experimental results from controlled blade tip/shroud rubs at engine speed. Journal of Turbomachinery Vol. 129, No. 4 (2006), 713–723. DOI: 10.1115/1.2720869.

[8] H. Doi and J. J. Alonso. Fluid/Structure Coupled Aeroelastic Computations for Transonic Flows in Turbomachinery. *ASME Turbo Expo 2002*. 2002, pp. 787–794. DOI: 10.1115/GT2002-30313.

[9] E. Petrov. Multiharmonic Analysis of Nonlinear Whole Engine Dynamics With Bladed Disc-Casing Rubbing Contacts. *ASME Turbo Expo 2012*. Vol. 44731. 2012, pp. 1181–1191. DOI: 10.1115/GT2012-68474.

[10] P. Almeida, C. Gibert, F. Thouverez, X. Leblanc, and J.-P. Ousty. Experimental analysis of dynamic interaction between a centrifugal compressor and its casing. Journal of Turbomachinery Vol. 137, No. 3 (2015), 031008. DOI: 10.1115/1.4028328.

[11] H. Ma, F. Yin, Y. Guo, X. Tai, and B. Wen. A review on dynamic characteristics of blade–casing rubbing. Nonlinear Dynamics Vol. 84, No. 2 (2016), 437–472. DOI: 10.1007/s11071-015-2535-x.

[12] A. Batailly, Q. Agrapart, A. Millecamps, and J.-F. Brunel. Experimental and numerical simulation of a rotor/stator interaction event localized on a single blade within an industrial high-pressure compressor. Journal of Sound and Vibration Vol. 375 (2016), 308–331. DOI: 10.1016/j.jsv.2016.03.016.

[13] F. Nyssen and A. Batailly. Investigations on thermo-mechanical modeling of abradable coating in the context of rotor/stator interactions. *ISROMAC - 17th International Symposium on Transport Phenomena and Dynamics of Rotating Machinery*.

[14] Q. Agrapart, F. Nyssen, D. Lavazec, P. Dufrenoy, and A. Batailly. Multi-physics numerical simulation of an experimentally predicted rubbing event in aircraft engines. Journal of Sound and Vibration Vol. 460 (2019), 114869. DOI: 10.1016/j.jsv.2019.114869.

[15] Y. Colaïtis and A. Batailly. The harmonic balance method with arc-length continuation in blade-tip/casing contact problems. Journal of Sound and Vibration Vol. 502 (2021), 116070. DOI: 10.1016/j.jsv.2021.116070.

[16] T. Vadcard, Y. Colaïtis, A. Batailly, and F. Thouverez. Assessment of Two Harmonic Balance Method-Based Numerical Strategies for Blade-Tip/Casing Interactions: Application to NASA Rotor 67. Journal of Engineering for Gas Turbines and Power Vol. 144, No. 12 (2022), 121004.

[17] T. Vadcard, F. Thouverez, and A. Batailly. Computation of isolated periodic solutions for forced response blade-tip/casing contact problems (2022). in Proceedings of the ASME Turbo Expo 2023.

[18] E. Rahimov, M. Watson, A. Hadjisoteriou, and M. Marshall. Investigation of wear mechanisms in AlSi-polyester abradable - Ti(6Al4V) blade contacts using stroboscopic imaging. Wear Vol. 494-495 (2022), 204207. DOI: https://doi.org/10.1016/j.wear.2021.204207.

[19] Y. Colaïtis and A. Batailly. Stability analysis of periodic solutions computed for blade-tip/casing contact problems. Journal of Sound and Vibration Vol. 538 (2022), 117219. DOI: 10.1016/j.jsv.2022.117219.

[20] H. Keller. Numerical methods in bifurcation problems. Lectures on Mathematics and Physics, Tata Institute of Fundamental Research (Bombay), 1987 (1987).

[21] E. P. Petrov. Analysis of Bifurcations in Multiharmonic Analysis of Nonlinear Forced Vibrations of Gas Turbine Engine Structures With Friction and Gaps. Journal of Engineering for Gas Turbines and Power Vol. 138, No. 10 (2016), 11.

[22] L. Xie, S. Baguet, B. Prabel, and R. Dufour. Numerical Tracking of Limit Points for Direct Parametric Analysis in Nonlinear Rotordynamics. Journal of Vibration and Acoustics Vol. 138, No. 2 (2016), 021007. DOI: 10.1115/1.4032182.

[23] T. Detroux, L. Renson, L. Masset, and G. Kerschen. The harmonic balance method for bifurcation analysis of large-scale nonlinear mechanical systems. Computer Methods in Applied Mechanics and Engineering Vol. 296 (2015), 18–38. DOI: 10.1016/j.cma.2015.07.017.

[24] R. Alcorta, S. Baguet, B. Prabel, P. Piteau, and G. Jacquet-Richardet. Period doubling bifurcation analysis and isolated sub-harmonic resonances in an oscillator with asymmetric clearances. Nonlinear Dynamics Vol. 98, No. 4 (2019), 2939–2960. DOI: 10.1007/s11071-019-05245-6.

[25] L. Xie, S. Baguet, B. Prabel, and R. Dufour. Bifurcation tracking by Harmonic Balance Method for performance tuning of nonlinear dynamical systems. Mechanical Systems and Signal Processing Vol. 88 (2017), 445–461. DOI: 10.1016/j.ymssp.2016.09.037.

[26] G. von Groll and D. Ewins. The Harmonic Balance Method with arc-length continuation in rotor/stator contact problems. Journal of Sound and Vibration Vol. 241, No. 2 (2001), 223–233. DOI: 10.1006/jsvi.2000.3298.

[27] E. Sarrouy and J.-J. Sinou. Non-Linear Periodic and Quasi-Periodic Vibrations in Mechanical Systems - On the use of the Harmonic Balance Methods. *Advances in Vibration Analysis Research*. Ed. by F. Ebrahimi. 2011. Chap. 21. DOI: 10.5772/15638.

[28] M. Urabe. Galerkin's procedure for nonlinear periodic systems. Archive for Rational Mechanics and Analysis Vol. 20, No. 2 (1965), 120–152. DOI: 10.1007/BF00284614.

[29] S. Narayanan and P. Sekar. *A frequency domain based numeric-analytical method for non-linear dynamical systems*. 1998. DOI: 10.1006/jsvi.1997.1319.

[30] S. Narayanan and P. Sekar. A frequency domain based numeric–analytical method for non-linear dynamical systems. Journal of sound and vibration Vol. 211, No. 3 (1998), 409–424.

[31] J. W. Cooley and J. W. Tukey. An algorithm for the machine calculation of complex Fourier series. Mathematics of Computation Vol. 19, No. 90 (1965), 297–301. DOI: 10.2307/2003354.

[32] D. C. Urasek, W. T. Gorrell, and W. S. Cunnan. *Performance of two-stage fan having low-aspect-ratio first-stage rotor blading*. NASA Lewis Research Center Cleveland, OH, United States. 1979.

[33] D. Laity. *Stage 67 rotor and stage 67 casing half stators mounted.* Records of the National Aeronautics and Space Administration, 1903 - 2006. Photographs relating to agency activities, facilities and personnel, 1973 - 2013.

[34] S. Kojtych and A. Batailly. A catalogue of open NASA blade models (2023).

[35] R. R. Craig Jr and M. C. Bampton. Coupling of substructures for dynamic analyses. AIAA journal Vol. 6, No. 7 (1968), 1313–1319. DOI: 10.2514/3.4741.

[36] A. Batailly, M. Legrand, P. Cartraud, and C. Pierre. Assessment of reduced models for the detection of modal interaction through rotor stator contacts. Journal of Sound and Vibration Vol. 329, No. 26 (2010), 5546–5562. DOI: 10.1016/j.jsv.2010.07.018.